Journal of Nuclear Materials 435 (2013) 17–24

Contents lists available at SciVerse ScienceDirect

Journal of Nuclear Materials

journal homepage: www.elsevier.com/locate/jnucmat

Photothermal microscopy applied to the characterization of nuclear fuel pellets

F. Zaldivar Escola [a,1], O.E. Martínez [b,2], N. Mingolo [a,*], R. Kempf [c]

[a] Universidad de Buenos Aires, Facultad de Ingeniería, Paseo Colon 850, 1063 Buenos Aires, Argentina
[b] Universidad de Buenos Aires, Facultad de Ciencias Exactas y Naturales Int., Güiraldes 2160, Pabellón I, Cdad. Universitaria, CABA C1428EAH, Argentina
[c] CNEA, Unidad Actividad Combustibles Nucleares, División Caracterización, San Martín, Pcia. de Buenos Aires, Argentina

HIGHLIGHTS

- Thermal diffusivity maps at the microscopic level are obtained.
- Histograms of the thermal diffusivity distribution quantify the homogeneity.
- Pore distribution and cluster detection of pure urania and gadolinea is achieved.
- Different fabrication protocols can be quantitatively compared.

ARTICLE INFO

Article history:
Received 28 June 2012
Accepted 5 December 2012
Available online 13 December 2012

ABSTRACT

The photothermal photodeflection technique is shown to provide information on the homogeneity of fuel pellets, pore distribution, clustering detection of pure urania and gadolinea and to provide a two-dimensional mapping of the thermal diffusivity correlated to the composition of the interdiffused Gadolinium and Uranium oxide. Histograms of the thermal diffusivity distribution become a reliable quantitative way of quantifying the degree of homogeneity and the width of the histogram can be used as a direct measure of the homogeneity. These quantitative measures of the homogeneity of the samples at microscopic levels provides a protocol that can be used as a reliable specification and quality control method for nuclear fuels, substituting with a single test a battery of expensive, time consuming and operator dependent techniques.

1. Introduction

It has long been recognized that the addition of gadolinium to UO_2 pellets extends the fuel cycles, increases burnup and optimizes power density distribution. The effect is due to the large neutron absorption cross section of gadolinium acting as a burnable poison at the beginning of the core life [1–3]. A burnable poison is a material used in reactors to provide a negative moderator coefficient at the beginning of reactor life and help shape core power distribution. It is added to a reactor core in order to burn out during mainly the first operating cycle; consequently the poison is consumed during operation and at the end of life, the burnable poison rod assembly is discharged [4].

Despite these advantages a deleterious effect appears in the sintering process limiting the amount of gadolinium that can be added, with the appearance of cracks, pores and gadolinea clusters that have to be kept below established levels [5].

The CNEA (Atomic Energy Agency from Argentina) has set up a project to design and build a small nuclear power plant named CAREM. The first stage is the construction and operation of the demonstration plant of about 27 MW, CAREM 25, to validate the technology and step forward towards the final development of the commercial versions. The development of manufacturing processes compatible with production requirements and quality restrictions gives rise to the need for detection and characterization techniques reliable, fast and inexpensive capable of determining as many relevant parameters as possible in a single test.

Usually, the UO_2–Gd_2O_3 pellets are prepared by sintering a mixture of mechanically blended powders of UO_2 and up to 10 wt.% of Gd_2O_3, and the obtained materials are expected to be mostly solid solutions of the $(U,Gd)O_2$ type [6].

In spite of the high sintering temperature (~1700 °C), inhomogeneous gadolinium distribution can occur and Gd_2O_3 clusters may be found at the sintered pellet. This is very undesirable, because Gd_2O_3 clusters will cause internal cracks and porosity in the pellets, which, in turn, will affect fuel performance and, eventually, cause fuel rod failure.

* Corresponding author.
E-mail addresses: facundozaldivar@hotmail.com (F. Zaldivar Escola), oem@df.uba.ar (O.E. Martínez), nmingol@fi.uba.ar (N. Mingolo), rodolfokempf@gmail.com (R. Kempf).

[1] Student fellow of CONICET, Argentina.
[2] Also Tolket SRL, Buenos Aires, Argentina and member of the technical staff of CONICET, Argentina.

0022-3115/$ - see front matter © 2012 Elsevier B.V. All rights reserved.
http://dx.doi.org/10.1016/j.jnucmat.2012.12.014

Differences of porosity and grain size are observed in the microstructure of sintered pellets, depending on the Gd content and its distribution. It is well known that the grain size diminishes as the Gd concentration increases. The sintered pellets present a mixture of UO_2 and other $(U,Gd)O_2$ phases with variable Gd concentration, with an inhomogeneous microstructure. The homogeneity characterization is then necessary for a production control to qualify the process and the final product. Several techniques have been used to probe the interdiffusion kinetics of gadolinium in the UO_2 matrix and the presence of non-exhausted gadolinia. In particular, X-ray diffraction and scanning electron microscopy have been the most frequent characterization techniques employed to analyze the chemical homogeneity in UO_2–Gd_2O_3 pellet [7].

Additionally a micrographic technique is performed to produce an image of the pellet surface. The sample has to be cut, polished and color etched; in the image the free gadolinia, urania and solid solution grains reflect different colors [7]. This analysis is time consuming and sensitive operator skills and has a tendency to overestimate the occurrence of free Gd_2O_3.

In this work photothermal deflection microscopy [8] is shown to provide information on the homogeneity of fuel pellets, pore distribution, clustering detection and provides a two-dimensional mapping of the thermal diffusivity distribution of the matrix, correlated to the composition of the interdiffused Gadolinium and Uranium oxide. As compared to prior characterization techniques this new method provides quantitative results, reducing the operator dependence of the micrographic techniques mentioned before. The technique will be presented in the next section, providing a detailed description of the data processing, the results in Section 3 and a discussion on the processed data in Section 4 with a final section with an enumeration of the conclusions.

2. Experimental

2.1. The photothermal technique

The experimental setup is described in detail in Ref. [9] and references therein. A pump laser emitting at $\lambda = 532$ nm is modulated at the desired frequency (between 30 kHz and 5 MHz) and is focused on the sample surface by means of a microscope objective. A probe laser emitting at $\lambda = 690$ nm is focused besides the pump about one spot size away and the reflection is detected by means of a photodiode after being clipped by the knife edge. A digital camera allows the precise focusing, observation of the sample and the measurement of the beam size. The signal is filtered by a lock-in amplifier in order to extract the modulated component both in amplitude and phase at the pump beam modulation frequency.

The technique used is based on a method reported before [8–10] consisting on heating the surface by a modulated laser beam and the simultaneous detection of the reflectance change [11–14], due to the temperature rise, and the deflection of the probe beam [15,16], due to the surface deformation caused by the localized thermal expansion, as described in Fig. 1. The deflection is sensed by intercepting part of the beam with a knife edge, generating in this manner a modulation of the detected signal as the beam oscillates laterally.

The photoreflectivity signal depends on the particular wavelength used for the probe beam, and eventually can be selected as to make this contribution negligible for particular materials. In a previous work [10] it was shown that if the contribution of the photodeflection is much larger than that of the change in reflectivity (as will be shown valid for this case), only the dominant mechanism needs to be taken into account and the detected signal

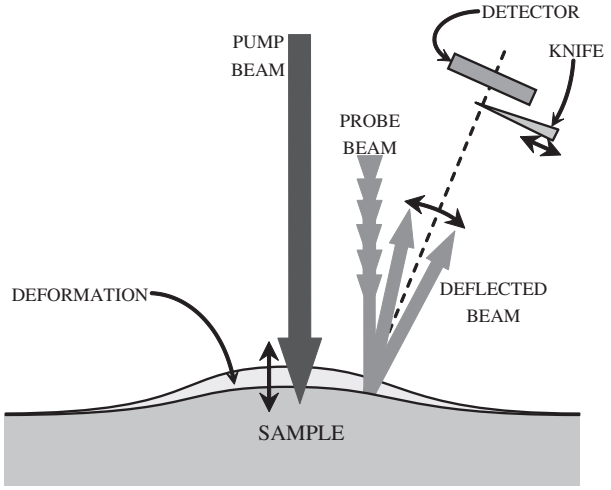

Fig. 1. Schematics of the mechanisms involved where it is shown that the surface expands due to the heat absorbed from the modulated pump laser and the deformation deflects the probe beam at the modulating frequency, thus modifying the power detected by the photodiode after being clipped by the knife.

(modulated component of the reflected probe at frequency ω) can be written as:

$$S_\omega = Bg(\omega/\omega_0) \tag{1}$$

with

$$B = P_P P_\omega R \left.\frac{d\tau}{dx_b}\right|_{x_b=0} \frac{z_f}{2\sigma} \frac{(1-R')}{\sqrt{2}\pi^2} \frac{\lambda_z}{\kappa_r} \tag{2}$$

where P_ω is the modulation depth of the pump power, P_p is the probe beam power, R is the reflectivity of the sample at the probe wavelength, R' is the reflectivity of the sample at the pump wavelength, τ is the transmission of the optical system between the sample and the detector, x_b is the beam center position at the knife edge plane, x_K is the knife edge position, z_f is the focal distance of the objective, σ is the incident spot size, λ_z is the thermal expansion in the z direction, K_r is the thermal conductivity parallel to the surface. B is a factor that depends on the material and beam size while g is a complex dimensionless function that depends on the beam separation and on the material only through the critical frequency $\omega_0 = 2\pi f_0$:

$$\omega_0 = \frac{2D_r}{\sigma^2} \tag{3}$$

where D_r is the thermal diffusivity parallel to the surface.

From the fit of the measured signal by Eq. (1) and using B and ω_0 as the adjustable parameters the critical frequency and hence the thermal diffusivity can be determined.

From Eq. (2) the material properties influencing the amplitude of the signal are the ratio of the thermal expansion coefficient divided by the thermal conductivity. For pure UO_2 pellets the ratio is 1.3×10^{-6} m/W [17,18] and for the sintered UO_2–Gd_2O_3 pellets it is even larger, around 2.8×10^{-6} m/W. These values are much larger than those for the materials used before with this technique [8–10] indicating that this material should be an excellent candidate for the method.

Fig. 2 shows a typical behavior of the frequency dependence of the amplitude and phase delay of the signal. In this case the phase of the complex signal depends only on the arguments of the function g in Eq. (1). Such arguments are only the beam sizes, shapes and separations, the modulating frequency and the thermal diffusivity (the only sample dependent coefficient). If the beams and modulating frequency are kept constant while scanning, the

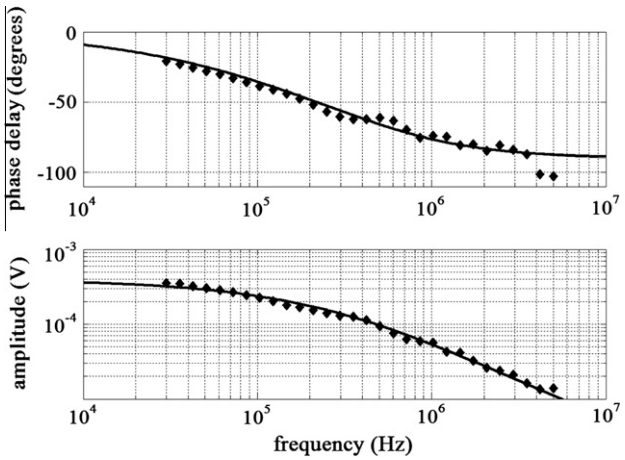

Fig. 2. Typical behavior of the frequency dependence of the phase delay and amplitude of the signal. Photodeflection is the dominant part in this case. From the fit a critical frequency $\omega_0 = 2\pi f_0$ is retrieved that corresponds to that at which the heat diffuses a length equal to the pump beam size in one modulation period.

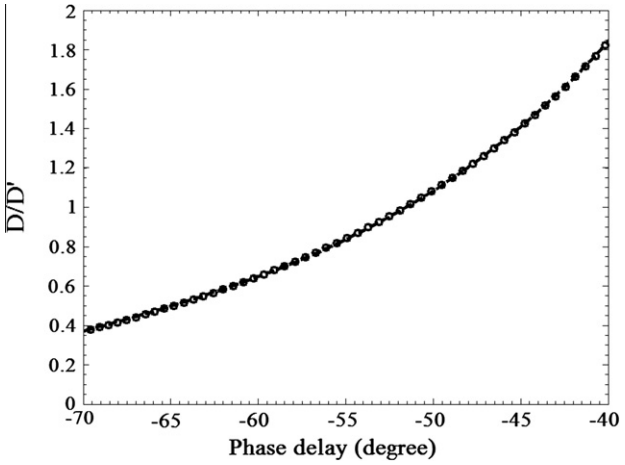

Fig. 3. Typical dependence of the normalized thermal diffusivity with the phase delay for a beam separation of 1.33 times the spot size. The calibration must be performed for the beam separation used.

change in the phase of the signal can only arise from a change in the thermal diffusivity. This fact can then be used to retrieve the thermal diffusivity by only measuring the phase delay at constant frequency, if the beam sizes and separations are also kept constant.

In Fig. 3 the thermal diffusivity, normalized to the diffusivity D' is plotted as a function of the phase delay. Where D' is defined by

$$D' = \frac{\omega\sigma^2}{2} \tag{4}$$

which corresponds to the thermal diffusivity that has its critical frequency ω_0 equal to the modulating frequency ω. In this particular case the pump–probe beam separation was 1.33 times the pump beam radius (a slightly different curve is obtained for different beam separations and must be computed again if the beam separation changes). The slope ranges between 3% and 9% per degree, indicating that small variations in the diffusivity yield large changes in the phase delay and hence by scanning the sample while measuring the phase delay it should be possible to map the thermal diffusivity variations with very high sensitivity. In this manner selecting a constant beam size and modulation frequency, the parameter D' is determined and scanning the sample at fixed beam separation from the plot of Fig. 3 the thermal diffusivity map can be constructed.

The procedure is to scan the surface at constant modulation frequency and building three images. One is the total reflected probe power which corresponds to the optical image of the sample (that can be also obtained with a digital camera installed in the setup), this two images are shown for an example in Fig. 4a (camera) and Fig. 4b (optical image), this example corresponds to a region of sample II described in Section 2.2. The other two images are the amplitude and phase delay of the photodeflection signal.

2.2. Samples

Two different batches of $(U,Gd)O_2$ pellets were produced and the samples obtained were named Type I and Type II. The $UO_2 + Gd_2O_3$ powders were blended by mixing the precursors in double cone blender, with an intensifier bar, rotating at 32 rpm, for 4 h. The UO_2 used to prepare all samples was an ex-ammonium uranyl carbonate powder with impurity content less than 150 ppm, specific surface area (BET) of 5.4 ± 0.1 m^2/g, average particle size of 8.6 ± 0.2 μm (Sedigraph), and O/U ratio of 2.05 ± 0.01. The Gd_2O_3 raw powder was of commercial grade (i.e., 99,9 % pure), with average particle size of 2.7 ± 0.2 μm, picnometry density 7 g/cm^3, specific surface area (BET) of 2.7 ± 0.1 m^2/g and was calcinated at 900 °C during 2 h before mixing.

The pellets were pressed in composition batches, where "green" pellets were obtained with pressure 300 MPa at ambient temperature. The pressing process was done in a floating table press, having green densities in the range 51–53% theoretical density.

The two different samples prepared differed in the sintering cycle as shown in Fig. 5. The sintering cycle was conducted under a 99.999% H_2 atmosphere, at a flow of 200 ml/min, in molybdenum furnace, raising the temperature up to 1650 °C during 2 h for Type I and 1750 °C for 8 h for Type II (Fig. 5). For comparison, one batch of pure UO_2 pellets was prepared.

For the photothermal characterization the samples were encapsulated and polished to obtain an optically flat and reflective surface. A microscopic image of a sample of Type I is shown in Fig. 6a, displaying a region of 612 μm × 458 μm. The pores appear clearly as dark regions. Fig. 6b shows a similar image obtained for a sample Type II. The reduced pore density and size is evident already with these images. The small frame in each image indicates the size of the area scanned by the photothermal technique, showing that the sampling is representative of the material under study.

The electronic bandgaps of uranium and gadolinium oxides are very different. UO_2 has a direct bandgap at 2.1 eV at room temperature which corresponds to a photon of λ = 590 nm [19,20] and the penetration depth is of the order or less than 1 μm for photons of 2.3 eV used as pump (λ = 532 nm). This provides an adequate fit to the basic theoretical assumptions for the model used, i.e. a penetration depth significantly smaller than the beam diameter (6 μm). This guarantees that the pump beam is absorbed in a thin layer much smaller than the thermal diffusion length. Conversely the gadolinea has a negligible absorption at these scales, with a direct electronic bandgap between 5 eV and 5.5 eV depending on the fabrication method [21,22] which falls in a wavelength range of deep UV (<250 nm). The gadolinea results transparent at the pump laser wavelength and hence produces no photothermal signal. This was verified measuring in a large gadolinea cluster found in one of the samples that could be identified directly by eye. The absence of photothermal signal was used as a way to identify pure gadolinea clusters larger than the optical resolution of the microscope. The UO_2 has a refractive index of n = 2.3 [23] yielding a reflectivity at normal incidence of 15%. Gadolinea has a refractive index between 1.75 and 1.9 [22,24], yielding a reflectivity between 8% and 10%. These values are too similar to be distinguishable by direct observation in the microscope.

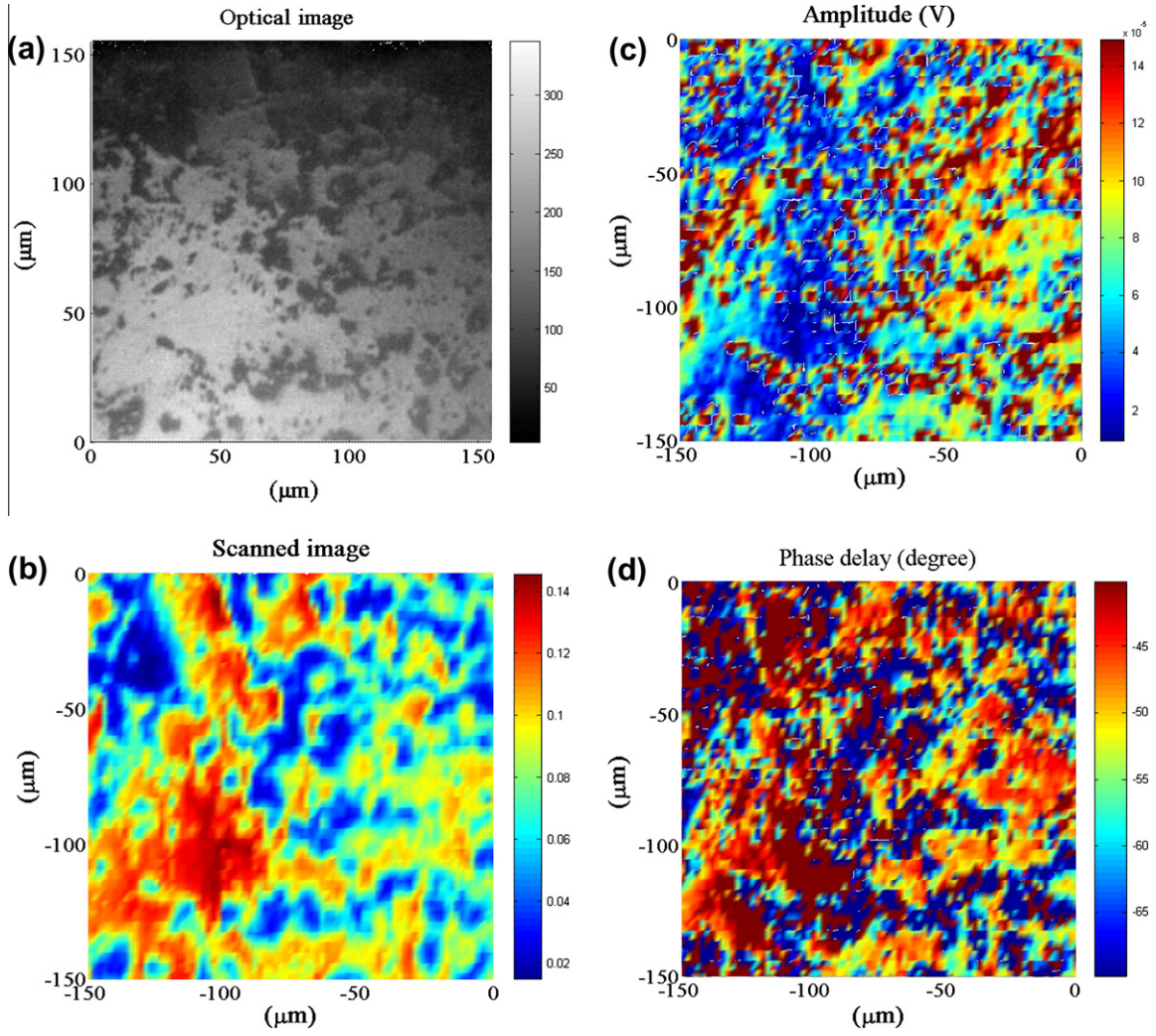

Fig. 4. Typical image obtained with the photothermal microscope. (a) Optical image with a camera, (b) scanned optical image obtained from the reflected probe beam, (c) amplitude of the photothermal signal, (d) phase delay of the photothermal signal.

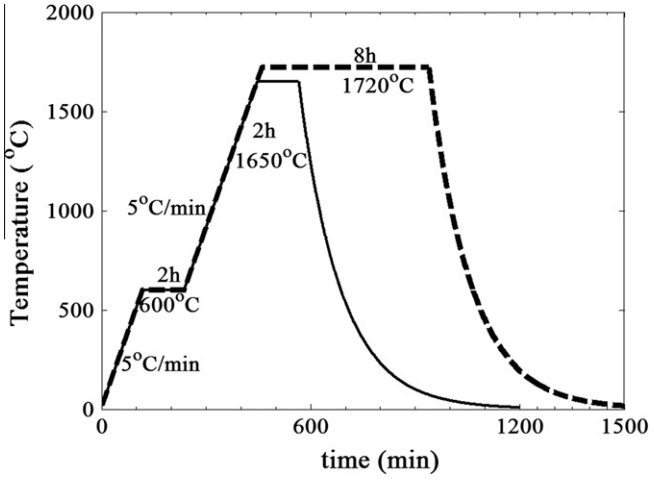

Fig. 5. Thermal cycle of the $UO_2 + Gd_2O_3$ sintered samples. Type I full line, Type II dashed line.

The use of the photothermal signal to distinguish the homogeneity of the sintered material relies in the following two facts: one is that urania and gadolinea have very different thermal diffusivities, with $D(UO_2) = 0.027\ cm^2/s$ [25,26] and $D(Gd_2O_3) = 0.118\ cm^2/s$, (measured by the flash method in a sample prepared for this purpose) and hence a mixture of the two materials should have a thermal diffusivity somewhere in between, i.e. larger than that of urania. The second one is that the interdiffused sample has a thermal diffusivity lower than that of urania as determined for samples with 10% Gd by the flash method [27,28], yielding $D(UO_2 + 10\% Gd_2O_3) = 0.0156\ cm^2/s$ which is more than 40% lower than urania, allowing the clear distinction between the mixture and the interdiffusion on one side and a determination of the homogeneity, as the method used has a resolution of about 5% (understanding by resolution the distinction within one scan, while accuracy is of about 15% and is a comparison with a standard).

3. Data processing

The system described in the experimental section acquires four images per scanned area. An example is shown in Fig. 4. Fig. 4a is the camera image of the region to be scanned. Fig. 4b is the reflected power of the probe beam and corresponds to an optical image (reflection) of the scanned region. This image has the resolution limited by the probe beam size (approximately 3 μm radius) while the camera image has the resolution of the objective (1.3 μm at the center) convolved with the pixel size (0.6 μm at

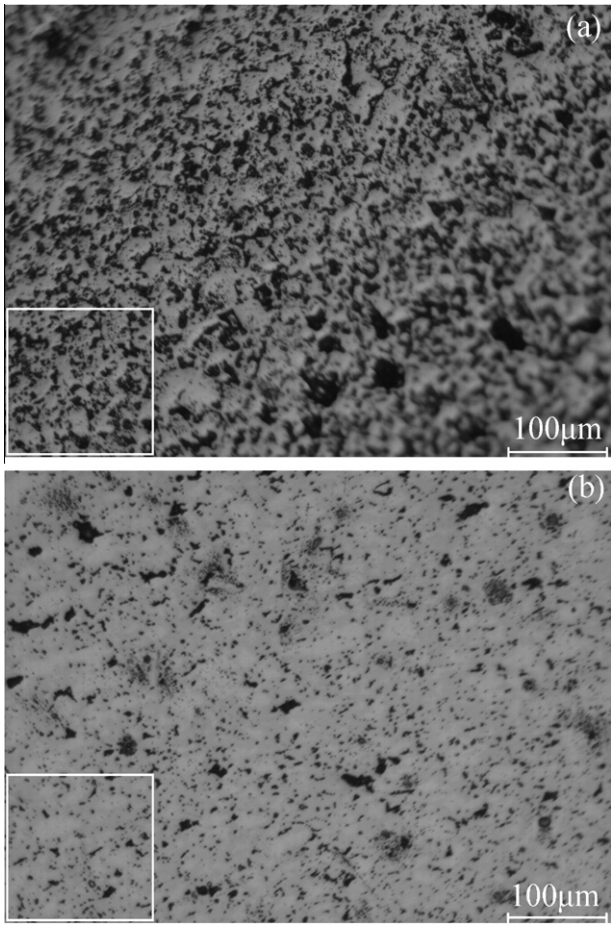

Fig. 6. Micrographs of the samples taken with a camera on an optical microscope. (a) Type I. (b) Type II. The inserted squares show the typical scan area for each photothermal image.

the sample). Fig. 4c and d are the amplitude and the phase angle delay of the complex photothermal signal provided by the lock-in amplifier at the modulation frequency.

The optical image Fig. 4b presents dark regions consistent with those of the camera picture Fig. 4a that corresponds to pores larger than the optical resolution. As mentioned before the gadolinea has a direct electronic bandgap at an energy corresponding to 250 nm photon wavelength [21,22] and does not absorb the radiation at the pump wavelength. Hence pure gadolinea will not heat with the pump laser and will not expand, yielding null amplitude in the signal as also seen at the pore locations. Consequently the amplitude image (Fig. 4c) has a very low value (within the noise level) for regions with pores or pure gadolinea. The regions with low reflectivity (Fig. 4b) will correspond to pores and the regions with low photothermal signal (Fig. 4c) will be the sum of the regions with pores and with pure gadolinea. Once the regions with pores and gadolinea are identified and deleted from the phase delay image, the remaining points will correspond to regions with a significant amount of UO_2. For these regions the procedure described in the previous section is used to retrieve the thermal diffusivity.

The procedure just described can be automated as follows: a threshold is defined for the reflectivity image (Fig. 4b) and the picture is binarized with ones above the threshold and zeros below. This binary image directly provides a map of pores in black. The result for this procedure applied to Fig. 4b is shown in Fig. 7a. A similar binarization is carried out with the amplitude image to reject the points with null signal arising from the non-absorbing sites

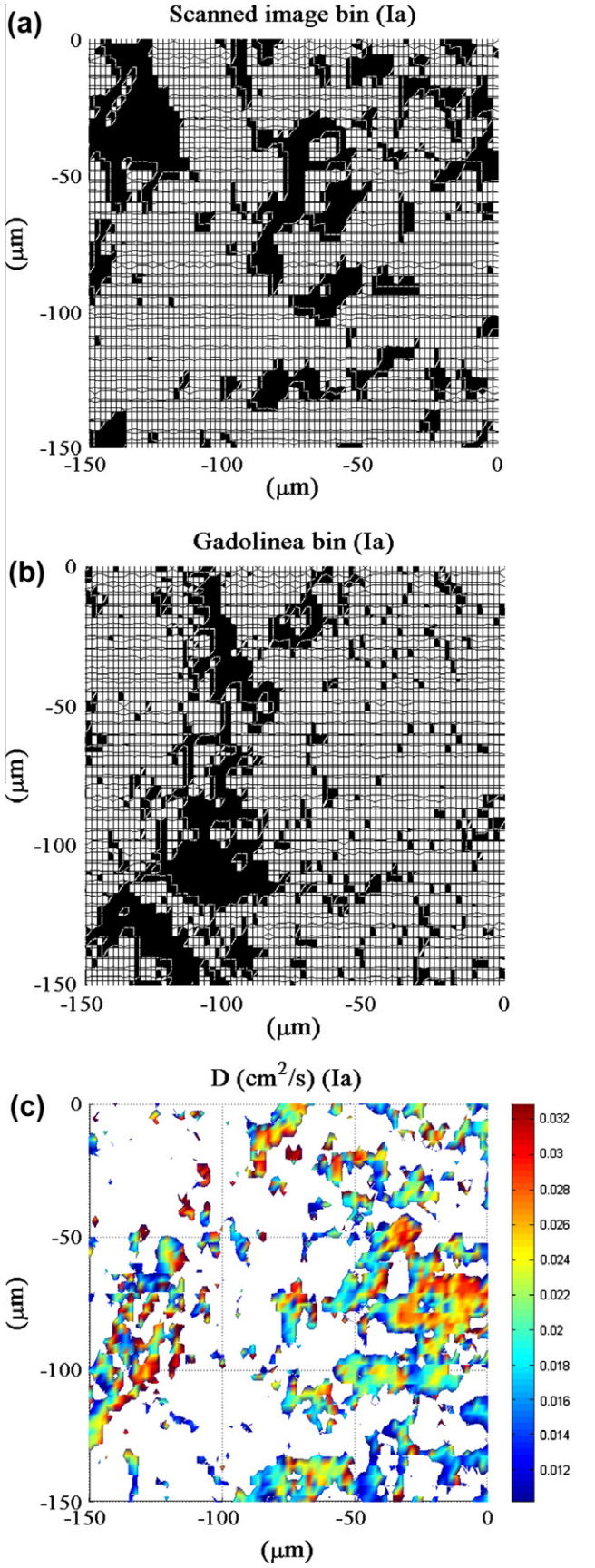

Fig. 7. Processed images from Fig. 4. (a) Pore locations (black) after binarization of the scanned optical image (Fig. 4b), (b) gadolinea clusters after binarization of the amplitude filtered by the pore location, (c) thermal diffusivity obtained by the curve of Fig. 3 after rejecting the points either with pores or gadolinea.

(pores and gadolinea). To choose the threshold for this second binarization the following algorithm was used: the signal from regions corresponding to pores where taken as background noise, for these zones a mean value of the amplitude and standard deviation were determined. The new threshold was established as the mean background value plus twice the background standard deviation, leaving in this manner 98% of the noise below the threshold. Similar signal levels (noise) are expected from the gadolinea regions that, as described before, should not yield any photothermal signal due to the lack of optical absorption of the pump beam. This new binarized image will have zeros where there is a pore or a gadolinea cluster and ones elsewhere. The inverse of this binarized figure (ones at the pores and gadolinea), when multiplied by the pore binarization, yields zeros everywhere except at the locations of the gadolinea clusters. Inverting this figure a map is obtained with zeros at the gadolinea locations (see Fig. 7b). The binarized amplitude image is then multiplied by the phase delay image yielding the retrieved phase delay everywhere except where there is a pore or a gadolinea cluster (zero in the binarized amplitude). From this filtered phase delay image the thermal diffusivity is retrieved as shown in Fig. 7c. All diffusivity maps for different samples are presented with the same color scale for ease of comparison.

3.1. Results

The procedure described in Section 3 was repeated in two regions of the two samples and for pure UO_2. The regions explored are denoted by Ia and Ib for Type I; IIa and IIb for Type II. Only the processed images for the pore and gadolinea localization and the thermal diffusivity for one of the samples (Ia) is presented. The first sample (Type I) was less homogeneous and had larger pores and gadolinea clusters. The processed results for sample Ia were already shown in Fig. 7a where the first image shows the pores in black after binarization of the reflectivity image. The pore area fraction was obtained from this figure and is depicted for all samples in Table 1 as percent of the surface with pores larger than the resolution of the beam (3 μm radius). Fig. 7b shows the binarized image with the location of the gadolinea clusters larger than the beam size, and the percentage occupied by gadolinea clusters are also shown in Table 1. Fig. 7c is the thermal diffusivity for the same region showing a large inhomogeneity.

A second region of the same sample denoted Ib presented similar results. The pores and gadolinea fraction for this region can also be found in Table 1.

Two regions for the second sample (Type II) were analyzed. Both showed smaller pores and gadolinea clusters. In the first region (IIa) a large cluster of higher diffusivity (Fig. 8) is observed with a background of smaller diffusivity. The larger diffusivity is consistent with the reported values for the UO_2 [25,26]. To check this hypothesis a pure UO_2 sample was scanned. The pore fraction (Table 1) resulted much smaller than that of the samples containing Gd. The very small fraction of gadolinea measured (Table 1) is an indication of the resolution of the technique, as obviously this sample has no gadolinea clusters and the false reading arises from noise.

Table 1
Pore and gadolinea fraction for two regions of samples I and II and for pure UO_2.

Sample	Pore fraction (%)	Gd_2O_3 fraction (%)
Ia	27 ± 8	26 ± 6
Ib	24 ± 3	8 ± 4
IIa	4 ± 0.3	1.28 ± 0.6
IIb	8.3 ± 2	1 ± 0.3
UO_2	2.5 ± 0.5	0.6 ± 0.3

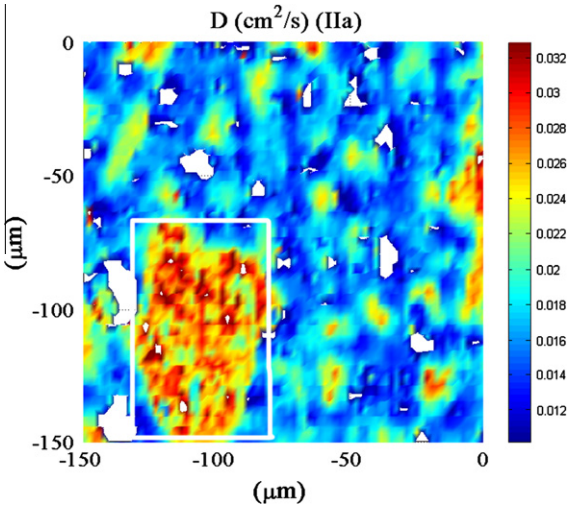

Fig. 8. Thermal diffusivity obtained from the calibrating curve of Fig. 3 after rejecting the points either with pores or gadolinea. The small frame indicated shows a cluster identified as urania (see Section 4).

4. Discussions

From the pore fraction analysis (Table 1) and the observation of the binarized pore maps (Fig. 7a, and similar figures for the other samples not shown) it can be concluded that the increase in the sintering temperature and longer duration has reduced the fraction and sizes of the pores.

The Gadolinea content was also substantially reduced (see Table 1) and the cluster sizes is also much smaller in sample II as was inferred from the observation of the corresponding images. In fact for sample II the gadolinea clusters content is very close to the detection limit of the technique, which is determined by the fraction of false positives identified in a sample without Gadolinium content (0.6% according to Table 1). False negatives can also appear for very small gadolinea grains as the technique has a spatial resolution determined by the pump laser beam size used (3 μm radius). It is possible to measure with smaller beam sizes provided that the modulating frequency is scaled according to Eq. (3).

The size distribution of the gadolinea clusters can be retrieved from the binarized images provided by the technique using standard image analysis.

For the analysis of the homogeneity of the remaining matrix, histograms of thermal diffusivity distribution were preformed for the thermal diffusivity maps as the ones shown in Figs. 7c and 8. The results for the mean value and standard deviation for all regions analyzed are presented in Table 2, together with the relative width (standard deviation divided by the mean value). In Fig. 9 the histogram for pure UO_2, one region of each samples I and II are depicted for comparison.

Table 2
Mean value, standard deviation and relative width from histograms of all samples. Where UO_2 pure denotes a sample prepared as reference. IA and IB are two regions of sample Type I. IIA, IIB, IIC are different regions of sample Type II; in particular IIA_cluster is an isolated region of region IIA shown in Fig. 8.

Sample description	Mean (cm^2/s)	Std (cm^2/s)	Std/mean
UO_2 pure	0.0297	0.0046	0.155
IA	0.0190	0.0097	0.51
IB	0.0185	0.0129	0.697
IIA	0.0185	0.0048	0.26
IIA_cluster	0.0260	0.0037	0.14
IIB	0.0194	0.0046	0.24
IIC	0.0248	0.0056	0.226

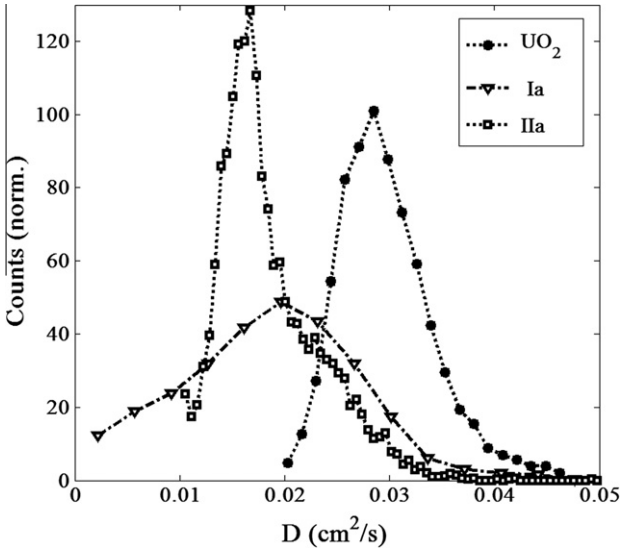

Fig. 9. Histogram of the thermal diffusivity obtained for the pure UO_2 sample and for the regions shown in Fig. 7c and 8 for samples Types I and II respectively.

The precision of the method as determined for calibrating samples of other materials is of 5% in the fluctuations of the retrieved thermal diffusivity after different tests at constant beam separation and beams sizes. The variations of the beam separations and sizes from day to day give rise to accuracy substantially worse than the precision, as an error of 10% in the beam separation (300 nm change) yields an 8% error in the thermal diffusivity. The beam size error also introduces an error as seen from Eq. (3), with a 10% incidence in the accuracy if a 5% error is made in the determination of the beam size. Hence measurements made in a single scan (same image) at constant beam sizes and separations should have an inherent width in the histogram of 5% and accuracy between 10% and 20% (absolute position of the mean value, i.e. calibration). The 15% width of the histogram shown in Fig. 9 for pure UO_2 can be attributed to real fluctuations in the sample arising probably form fluctuations in the grain and nanopores sizes that act as thermal barriers reducing the diffusivity value. In fact as the thermal wave diffuses into the material, the presence of pores were the wave is multiply scattered yield an effective medium of smaller diffusivity than the defect free material, and a dispersion in pores distribution hence broadens the histogram.

From the precision of 5% in the determination of relative changes in the thermal diffusivity within one image, being the thermal diffusivity proportional to the critical frequency (Eq. (3)) and as our electronics can scan a range from 30 kHz to 5 MHz, the contrast of the technique as installed has a contrast in the determination of the thermal diffusivity of

$$C = \frac{1}{0.05} \ln\left(\frac{f_{max}}{f_{min}}\right) \cong 100 \tag{5}$$

As the maximum and minimum diffusivities that can be measured scales with the pump beam area, the dynamic range of the measurement shifts with the spatial resolution, that is determined as discussed before by the pump beam size. For the beam size used in our experiments (3 μm radius) the thermal diffusivity span of the instrument as set is 8×10^{-3} cm^2/s to 1.4 cm^2/s.

To evaluate the effect of day to day fluctuations in the beam sizes and separations, two images were taken of the same region denoted by samples IIb and c (images not shown). The results are presented in Table 2. As discussed before the same width appeared in both scans but with a different location of the mean value, shifted by 22%. The relative width of the histograms is larger than that of pure UO_2, which is expected from the additional disorder provided by the presence of another fluctuating parameter (composition). This shows that the histograms widths are reliable and the absolute value retrieved for the thermal diffusivity has an error of the order of 20%.

The analysis of the histograms also shows clearly that two regions of the same sample have similar widths (homogeneities) and that sample II is substantially more homogeneous than sample I (see relative widths in Table 2).

In particular it should be noticed that one of the histograms in Fig. 9 (corresponding to the image of Fig. 8) is quite asymmetric with the appearance of a two lobe distribution. From the observation of Fig. 8a cluster of high thermal diffusivity is easily recognized and indicated with a rectangular frame. Performing a histogram in the frame area a diffusivity value shifted towards that of pure UO_2 is found (IIA_cluster in Table 2) with a width identical of that obtained for the pure sample (see Fig. 9). This result allows us to identify this cluster as composed of almost pure UO_2.

5. Conclusions

It has been shown that the photothermal photodeflection technique provides thermal diffusivity maps at the microscopic level in ceramic samples of nuclear interest. The microscopic map of the thermal diffusivity was shown to be a powerful way of determining the homogeneity of the fabricated sample. Histograms of the thermal diffusivity distribution are a reliable quantitative way of quantifying the degree of homogeneity and the width of the histogram can be used as a direct measure of the homogeneity.

As the thermal diffusivity of the interdiffused $(U,Gd)O_2$ phases is much lower than any of the pure oxides, the technique can distinguish inter-diffused material from conglomerates of pure gadolinea and urania nanoparticles, even in the case this particles are much smaller than the optical resolution of the microscope. In fact such mixtures would have thermal diffusivities larger than that of urania. Such information at microscopic level could only be acquired for similar samples with a delicate and time consuming electron back scattering diffraction experiment.

The technique not only determined the thermal diffusivity but also in the same scan was able to localize, quantify and measure the microscopic and mesoscopic pores providing the relative area they occupy. Similar measurements of gadolinea clusters were performed due to the distinct electronic bandgap of gadolinea as compared to urania. Using green pump laser light the urania phases were strongly absorbent, providing a large photothermal signal while gadolinea did not absorb and hence gave a null signal that was used to identify its presence.

Due to the lower thermal diffusivity of interdiffused uranium and gadolinium oxides as compared to pure gadolinea and urania, the technique can establish if the sintering process yielded a homogeneous interdiffused sample or else if there is a mixture of grains. Clusters of urania grains with low or null gadolinium content were also identified in this manner.

The comparison of samples manufactured with different procedures allowed a clear identification of the improvements obtained after changing the fabrication protocol.

Finally it can be stressed that as the technique provides quantitative measures of the homogeneity of the samples at microscopic levels, it provides a protocol that can be used as a reliable specification and quality control method for nuclear fuels.

Acknowledgements

The authors wish to acknowledge grants from UBACyT and ANPCyT.

References

[1] W. Böhm, H.D. Kiehlmann, A. Neufert, M. Peehs, Kerntechnik 50 (1987) 234–240.
[2] E. Hellstrand, Trans. Am. Nucl. Soc. 40 (1982) 181–185.
[3] F.B. Skogen, L.A. Nielsen, R.G. Grummer, Trans. Am. Nucl. Soc. 40 (1982) 194–198.
[4] H. Assman, J.P. Robin, Guidebook On Quality Control Of Mixed Oxides And Gadolinium Bearing Fuels For Light Water Reactors, IAEA-TECDOC-584, IAEA, Viena, Austria, 1983.
[5] M. Durazzo, F.B.V. Oliveira, E.F. Urano de Carvalho, H.G. Riella, J. Nucl. Mater. 400 (2010) 183–188.
[6] TECDOC-844, International Atomic Energy Agency, Characteristics and Use Of Urania-Gadolinia Fuels, ISSN 1011–4289, Viena, Austria, 1995.
[7] L. Hälldahl, S. Eriksson, J. Nucl. Mater. 153 (1988) 66–70.
[8] O.E. Martínez, F. Balzarotti, N. Mingolo, Appl. Phys. B 90 (2008) 69–77.
[9] U. Crossa Archiopoli, N. Mingolo, O.E. Martínez, Surf. Coat. Technol. 205 (2011) 3087–3092.
[10] 10.U. Crossa Archiopoli, N. Mingolo, O.E. Martínez, J. Appl. Phys. 107 (2010) 023520-1–023520-6.
[11] Li Bincheng, J.P. Roger, L. Pottier, D. Fournier, J. Appl. Phys. 86 (1999) 5314-1–5314-3.
[12] D. Fournier, MRS Bull. 26 (2001) 465–470.
[13] D. Rochais, H. Le Houëdec, F. Enguehard, J. Jumel, F. Lepoutre, J. Phys. D 38 (2005) 1498–1503.
[14] A. Rosencwaig, J. Opsal, W.L Smith, D.L Willenborg, Appl. Phys. Lett. 46 (1985) 1013–1015.
[15] A. Rosencwaig, J. Opsal, D.L. Willenborg, Appl. Phys. Lett. 43 (1983) 166–168.
[16] Opsal, A. Rosencwaig, D.L. Willenborg, Appl. Opt. 22 (1983) 3169–3176.
[17] D.G. Martin, J. Nucl. Mater. 152 (1988) 94–101.
[18] Yu.K Bibilashvili, A.V. Kuleshov, O.V. Milovanov, E.N. Mikheev, V.V. Novikov, S.G. Popov, V.N. Proselkov, Yu.V. Pimenov, Yu.G. Godin, Investigation of thermal-physical and mechanical properties of uranium-gadolinium oxide fuel, IAEA-TECDOC-1416. Proceedings of a Technical Committee Meeting Brussels, 2003, pp. 85–100.
[19] T.R. Griffiths, H.V.St.A. Hubbard, J. Nucl. Mater. 185 (1991) 243–259.
[20] P. Ruello, K.D. Becker, K. Ullrich, L. Desgranges, C. Petot, G. Petot-Ervas, J. Nucl. Mater. 328 (2004) 46–54.
[21] M.P. Singh, C.S. Thakur, K. Shalini, S. Banerjee, N. Bhat, S.A. Shivashankar, J. Appl. Phys. 96 (2004) 5631–5637.
[22] N.K. Sahoo, S. Thakur, M. Senthilkumar, D. Bhattacharyya, N.C. Das, Thin Solid Films 440 (2003) 155–168.
[23] R.J. Ackerman, R.J. Thorn, G.H. Winslow, J. Opt. Soc. Am. 49 (1959) 1107–1112.
[24] A.A. Dakhel, J. Opt. A: Pure Appl. Opt. 3 (2001) 452–454.
[25] J.K. Fink, J. Nucl. Mater. 279 (2000) 1–18.
[26] C. Ronchi, M. Sheindlin, M. Musella, G.J. Hyland, J. Appl. Phys. 85 (1999).
[27] Mutsumi Hirai, J. Nucl. Mater. 173 (1990) 247–254.
[28] M. Amaya, M. Hirai, H. Sakurai, K. Ito, M. Sasaki, T. Nomata, K. Kamimura, R. Iwasaki, J. Nucl. Mater. 300 (2002) 57–64.